Composites Science and Technology 245 (2024) 110304

Contents lists available at ScienceDirect

Composites Science and Technology

journal homepage: www.elsevier.com/locate/compscitech

Predicting mechanical and electrical failure of nanowire networks in flexible transparent electrodes

Davide Grazioli *, Gabriele Gangi, Lucia Nicola, Angelo Simone

Department of Industrial Engineering, University of Padova, Padua, Italy

ARTICLE INFO

Keywords:
Metal nanowire electrodes
Electrical properties
Mechanical properties
Finite element analysis (FEA)
Computational mechanics

ABSTRACT

Flexible transparent electrodes employing metal nanowires (NWs) find extensive use in various applications such as optoelectronic devices, solar cells, light-emitting diodes, and transparent heaters. NW networks in flexible transparent electrodes can withstand mechanical deformations and conduct electricity but are susceptible to localized damage caused by mechanical stress and current density concentration. This localized damage ultimately results in electrode failure. Our study aims to track locally induced damage from both mechanical and electrical sources and assess their collective influence on electrode performance until failure occurs. To this end, we create two-dimensional digital samples that represent the NW networks, transform them into beam networks and equivalent resistor networks, and perform finite element simulations of the mechanical and electrical network responses while varying the NW content.

Our simulations reveal crack-like patterns in the distribution of damaged elements at network failure that depend on the process inducing the damage. While our results suggest that the impact of electrically induced damage on overall network stability is more significant than that of mechanically induced damage, the latter must not be ignored.

1. Introduction

Metal nanowires (NWs) arranged in network structures have been found to be appropriate for the fabrication of flexible transparent electrodes. These metal NW electrodes exhibit both transparency and electrical conductivity comparable to those of commercial thin film electrodes, making them suitable for various applications, the most common being optoelectronic devices such as touchscreens and flat panel displays, solar cells, light emitting diodes, and transparent heaters for defrosting and heating applications [1–4]. Compared to thin films, metal NW electrodes possess excellent mechanical flexibility, making them ideal for deformable applications as well. Examples of such applications include flexible displays, sensors, wearable devices, and stretchable electronics [1,3]. The unique characteristic of metal NW electrodes lies in the interplay between their local (NW level) and global (network level) responses, which ultimately rely on the integrity of the NWs. The failure of a single NW alters the local response of the network and can trigger a cascade of further failures in a loop that affects the network local and global responses [1]. The relationship between the damage of NWs and the resulting impact on the electrical and mechanical functionality of the electrode is the focus of this contribution.

The fabrication of a metal NW electrode entails the random deposition of NWs on a substrate and a post-treatment welding strategy [3]. The latter is performed to provide NW connections (junctions) with desirable mechanical and electrical properties. The electrode enables electrical current conduction only if the NW assembly creates a NW network. Such a condition is statistically fulfilled if the amount of NW exceeds a minimum content, the so-called critical percolation [5] (or percolation threshold). The existence of a NW network also ensures that the collective response of the NWs accommodates the macroscopic deformation of the electrode through a load bearing mechanism analogous to that of beam frames. At variance with these structures, the NW network is an entangled assembly of NWs that exert constrains on the displacement of the surrounding NWs. As a consequence, simple macroscopic deformation modes (electrode bending and stretching) induce complex deformation regimes (combination of tension/compression, bending, twisting and torsion) on the NWs [6–10].

The structure of the NW network is not static: it evolves and deteriorates during service. A NW subject to sufficiently high electric current levels breaks either due to Joule heating or electromigration [11–13]. In NW electrodes, the random arrangement of the NWs [14] and local fluctuations of the NW density [15,16] make the electric current

* Corresponding author.
E-mail addresses: davide.grazioli@unipd.it (D. Grazioli), gabriele.gangi@studenti.unipd.it (G. Gangi), lucia.nicola@unipd.it (L. Nicola), angelo.simone@unipd.it (A. Simone).

https://doi.org/10.1016/j.compscitech.2023.110304
Received 30 April 2023; Received in revised form 8 September 2023; Accepted 9 October 2023
Available online 12 October 2023

distribution highly inhomogeneous. Experimental evidence shows that electric current levels attained in some network locations are sufficient to cause NW breakages during standard electrode operations [16–19]. Mechanical stress and deformation similarly lead to NW breakage [20–26]. Several experimental investigations report about fractured NWs in electrodes undergone about 2%–3% strain when subject to either repeated bending cycles [6–9,15,27,28] or tensile test [10]. Tensile fracture [10], buckling [7,10,29], and bending [10,27] have been identified as the dominant failure mechanisms within the NWs. Significant strain localization, equally resulting in network breakage, has been observed in close proximity of the junctions [6–10,27]. Electrically and mechanically induced damage result in network connectivity losses that alter the macroscopic response of the electrode. Both types of damage determine electrode failure when a continuous pathway across the NW deposition no longer exists.

The sheet resistance is the property typically monitored during electrode stability analyses [6–10,15,17,18,27–33] because it reflects the state of health of the NWs. Indeed, as the breaking of NWs results in alteration of the NW network a sheet resistance rise is observed. Charvin et al. [32] conducted a study that combines experimental and computational methods to assess the impact of electrically induced NW failure on electrode stability. The study reports a non-linear relationship between the number of NW ruptures and the sheet resistance of the electrode. Mechanically induced failures can equally affect the overall response of flexible transparent electrodes [6–10,15,27,29–31,33]. Nevertheless, the authors are not aware of any previous attempts to investigate the relationship between mechanically and electrically induced damage and the resulting impact on the mechanical and electrical functionality of NW networks. Such a study could provide valuable insights into the degradation mechanisms that are most relevant to electrode failure.

To this end, we carry out two-dimensional numerical simulations on numerically generated distributions of one-dimensional objects representing NW electrodes. A Monte Carlo approach is pursued. The numerical realizations are converted into networks of beam [34,35] and resistor [36] elements. The former is employed to simulate the mechanical response of NW electrodes undergoing in-plane tensile deformations and determine the corresponding distribution of stresses. The latter is employed to simulate the electric current conduction processes and determine the electric current distribution throughout the network. Electrical damage evolution analyses are performed by replicating the approach pursued by Charvin et al. [32], which is here extended to enable the analysis of mechanical damage evolution (Section 2.1). In particular, we compute the mechanical stresses in each NW of the network while a macroscopic deformation is applied on the electrode. The location more likely to fail is therefore identified. We select the in-plane effective stiffness and the electrical conductivity of the electrode as indicators of the electrode mechanical and electrical functionalities, respectively. Although mechanical and electrical damage analyses are performed independently (no coupling effects are considered in the simulations), the effective stiffness and effective electrical conductivity are both evaluated during each damage analysis (Sections 2.1 and 2.2). A parametric study is performed (Section 4.1) ahead of the damage analyses to determine how the in-plane effective stiffness of pristine electrodes depend on NW content of the electrode, NW cross-sectional shape, and flexural stiffness of the junctions. A similar investigation is considered unnecessary for the effective electrical conductivity because a rich body of literature already describes analogous relationships (*e.g.*, Refs. [14,32,37–39]).

The results reported in Section 4.2 show that the distribution of damaged NWs is consistent with cracks patterns identified in experimental tests [15,16,18,19,27,31–33,40]. From the spatial analysis of these patterns we conclude that it is not possible to identify the NWs more likely to fail based on the visual inspection of the NW assembly. This is because there is no direct correlation between the arrangement of the NWs and the locations of damaged NWs resulting from the application of mechanical and/or electrical loads on the NW electrode. Furthermore, the results highlight an inherent difference between mechanical and electrical responses. The primary variable of the mechanical analysis is the displacement field, a vectorial field, while the primary variable of the electrical analysis is the electric potential, a scalar field. As a consequence, the 'flows' of mechanical stresses and electric current follow different patterns and result in different spatial distributions of the damaged NWs. This evidence allow us to concluded that both mechanical and electrical assessments are, in general, required. The results presented in Sections 4.3 and 4.4 show that the electrically induced damage is the most critical for the network performance because it results in a more pronounced mechanical and electrical functionality decay compared to the mechanically induced damage (for equal number of NW failures).

Table 1
Geometrical properties of AgNWs.

characterization	reference	diameter (nm)	length (μm)
	this study	100	15
electrical/optical	Charvin et al. [32]	70 ± 10	8 ± 3
	Gomes da Rocha et al. [38]	50	6.7
	Khaligh et al. [17]	90	25
	Kim et al. [41]	62.5	13.5
	Kim and Nam [42]		31.9
	McCarthy et al. [43]	54–78	1–50
	Nguyen et al. [15]	79 ± 10	7 ± 3
	Papanastasiou et al. [16]	70 ± 10	8 ± 3
	Sannicolo et al. [18]	79 ± 10	7 ± 3
	Sun et al. [44]	30–60	1–50
	Waliullah et al. [13]	53–173	
	Zhu et al. [19]	54	39
mechanical	Aghazadehchors et al. [31]	90	10–20
	Batra et al. [12]	65–195	15–60
	Chang et al. [45]	30–170	
	Filleter et al. [22]	40–120	~ 5–10
	Hu et al. [29]	60	5-15
	Hwang et al. [6]	62.5	13.5
	Hwang et al. [7]	~ 100	~ 15
	Hwang et al. [8]	35	
	Jing et al. [46]	40–120	
	Kim et al. [9]	20	18.5
	Lee et al. [27]	35	15
	Liu et al. [28]	25	25
	Noh et al. [33]	197.5	20.9
	Ojeda et al. [26]		2.5–10.5
	Poblete et al. [25]	~ 60	7.3–20.3
	Schrenker et al. [10]	35–85	tens of μm
	Vlassov et al. [23]	76–211	
	Wu et al. [20]	16–35	
	Xu and Zhu [30]	90	10–60
	Zhu et al. [21]	34–130	2.09–5.73
	ACS Material[a] [47]	23–120	13–200
	Novarials[a] [48]	10–200	5–200
	Sigma-Aldrich[a] [49]	20–200	6–40

[a] Commercial product. Geometrical description according to producer specifications.

2. Numerical modeling of nanowire networks

We focus on silver NWs (AgNWs) because a rich body of literature is devoted to their characterization, and because both geometrical and material properties are readily available. The approach is however general and the main conclusions extend readily to analogous scenarios. Typical values of AgNWs length and diameter are listed in Table 1. We limit our study to AgNWs with length $l_w = 15$ μm and effective diameter $d_w = 100$ nm, where the effective diameter indicates the diameter of the circle that circumscribes the NW cross section.

The mechanical response of NWs and junctions is dictated by their structure, shaped by synthesis and welding processes, respectively. AgNWs synthesized by the polyol method, for example, possess a peculiar fivefold twinned structure with five twin boundaries parallel

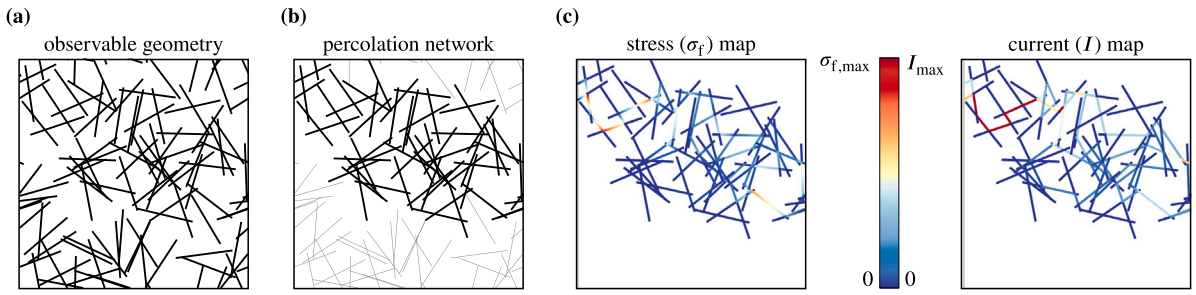

Fig. 1. Representative as-generated geometry, alternatively indicated as 'observable geometry' [14], at NW density $n = 6$ and domain size $L = 4\,l_w$ (a) with the corresponding percolation network (black lines) (b) and solution fields in terms of stress and current maps in the NWs (c).

to their axis (they are hence called 'penta-twinned AgNWs') [44]. Homogeneous NWs are known to have a size dependent elastic [50] as well as plastic [51] response caused by the increasing relevance of surface tension for decreasing diameter. Additionally, penta-twinned NWs have size effects caused by their special geometry [52], which is characterized by the presence of a disclination centered in the longitudinal axis. These effects appear to be negligible for diameters larger than 100 nm [21,23,45,46,52] and will be therefore disregarded. In this study, we make the assumption that NWs are homogeneous, are subject to quasi-static loads, and undergo small deformations in accordance with linear elasticity.

Experimental characterization indicates that the aspect ratio (l_w/d_w) of metal NWs is on the order of 100 or higher (according to the values of d_w and l_w listed in Table 1). As such, it is appropriate to model these NWs as one-dimensional beams, where flexural and shear deformations are accounted for through the application of the Timoshenko beam theory. We also account for axial deformation.

In modeling NWs, we utilize the following simplifying assumptions:

1. NWs are represented as straight widthless objects of constant length l_w endowed with identical cross-sectional shape and area A_w;
2. all material properties are considered constant along the NW axis;
3. the diameter of the NWs used in the analysis is sufficiently large such that both elastic and plastic size effects can be considered negligible;
4. the mechanical damage analysis of the NW network is conducted under the assumption that the NWs exhibit a brittle mechanical response;
5. the contacting NWs are welded together, and the weld between contacting NWs is called a 'junction';
6. a junction is a point-like constraint connecting the NWs (no attempt is made to explicitly describe its physical structure).

Although a distribution of lengths would provide a more realistic representation of actual NW ensembles (see Refs. [19,41,53], among many others), we aim to limit the variables to those strictly necessary and therefore assume that all the NWs have the same length l_w. An investigation into the effect of a non-uniform length distribution of rod-like fillers on the percolation threshold and electrical conductivity of the network can be found, for example, in Ref. [54].

To generate the numerical geometries, we adopt the methodology presented in Ref. [14] and produce two-dimensional structures referred to as 'observable geometries', according to the terminology used in the reference. Numerical simulations are conducted on two-dimensional samples of size $L \times L$ in which the NW content is defined by means of the NW density

$$n = N_w \frac{l_w^2}{L^2}, \tag{1}$$

where N_w indicates the number of NW in the simulation domain. Since some NWs in the observable geometries are either isolated or form isolated clusters (refer to Fig. 1a for an example of observable geometry), we focus solely on the percolation network (Fig. 1b) which consists of the subset of NWs involved in both electric current conduction and mechanical stress distribution processes. For detailed information regarding the generation of observable geometries and the process of identifying percolation networks, please refer to section S1 of the Supplementary material (Appendix A). For the sake of clarity, the definitions of the terms most frequently used throughout this work are given below. In this context, we use the term 'stick' to represent a simplified form of a NW as a one-dimensional straight object. A 'NW segment' refers to the section of a NW that is identified by two adjacent junctions, essentially where the stick intersects with two other sticks. Within the context of this work, the terms 'beam' and 'resistor' correspond to mathematical models utilized for simulating the mechanical and electrical responses of a NW, respectively.

To investigate mechanical and electrical properties of the network, numerical simulations are carried out. Mechanically and electrically induced damage, which will be referred to as 'mechanical damage' and 'electrical damage' respectively from here on, are analyzed separately and their mutual influence is investigated by means of a loosely coupled approach. Both investigations are based on the same underlying assumptions: i) damage occurs in the element where the stress (either electrical or mechanical) is maximum among all elements in the network, ii) damaged elements make negligible contributions to the overall response, and iii) elements in the network undergo damage sequentially, one at a time. When damage leads to the breakdown of the percolation network, the electrode fails and its mechanical strength and electrical conduction capability decay to zero. Therefore, we constantly monitor the percolation network during the damage evolution assessment procedures. Additional information about the numerical simulations is provided in the next sections.

2.1. Mechanical damage characterization

We assume that NWs deform in the plane of the network and neglect stress contributions arising from torsional and out-of-plane deflections. In order to determine the in-plane effective stiffness E_{eff} of the NW electrode and to carry out the mechanical damage analysis, we convert the percolation network into a beam network using the method described in section S4 of Appendix A. A similar approach is used in Refs. [34,35,55] to model the mechanical response of porous fibrous materials employed as substrates in battery electrodes.

Among the experimental characterization strategies employed to assess the mechanical stability of NW electrodes, tensile test is a viable option [10,29,30,33]. We simulate in-plane tensile load tests and evaluate the in-plane effective stiffness as

$$E_{eff} = \frac{F L}{t W \Delta L}, \tag{2}$$

which is understood as the effective property that relates the extent of the network elongation ΔL to the magnitude of the force F (parallel to the elongation) that induces it. With L, W, and t we indicate the length

of the domain along the elongation direction, the width of the domain in the direction orthogonal to the elongation, and the out-of-plane thickness, respectively. The product tW indicates the cross-sectional area of the electrode. The (generalized) internal forces (axial N and shear T forces, and bending moment M) in each beam element are computed through standard post-processing procedures [56]. Further details are provided in sections S1 and S4 of Appendix A.

The experimental characterization of AgNWs reveals a broad spectrum of potential mechanical behaviors, spanning from brittle [20,21,24] to ductile [10,22–24]. We assume that the material response of the NW is elastic up to failure, in agreement with the modeling assumptions adopted by Poblete et al. [25] and Ojeda et al. [26] for the interpretation of experimental tensile tests performed on AgNWs.

In structural integrity analysis, it is common practice to utilize a scalar measure of the local stress field and define a failure criterion based on it. To follow a similar approach, we adopt the local stress measure

$$\sigma_{\mathrm{f}}^2 = \sigma^2 + \alpha_{\mathrm{f}}^2\,\tau^2,$$

to identify failed NW segments, where σ and τ represent the axial and shear stresses, respectively, at any location on a generic cross section that is perpendicular to the beam axis.

We utilize the Guest-Tresca criterion and therefore use $\alpha_{\mathrm{f}} = 2$. Indicating with N and M the axial force and bending moment acting on a NW cross section, respectively, the axial stress is computed as

$$\sigma = \frac{N}{A_{\mathrm{w}}} - \frac{M}{I_{\mathrm{w}}}y,$$

where the coordinate $y \in [-d_{\mathrm{w}}/2, d_{\mathrm{w}}/2]$ quantifies the distance from the neutral axis of the cross section. The shear stress on a NW cross section caused by the shear force T acting on it is assumed to be equal to

$$\tau = \frac{T}{A_{\mathrm{w}}}.$$

The maximum value of σ_{f} on a beam element is thus

$$\sigma_{\mathrm{f}} = \sqrt{\left(\frac{|N|}{A_{\mathrm{w}}} + \frac{|M|}{I_{\mathrm{w}}}\frac{d_{\mathrm{w}}}{2}\right)^2 + 4\left(\frac{T}{A_{\mathrm{w}}}\right)^2}.$$

Applying this procedure to all beam elements in the network, we detect the maximum σ_{f} value for any cross section of any beam element.

The mechanical damage analysis starts with the 'undamaged beam network' representing the percolation network. The element with the maximum value of σ_{f} is identified and removed from the beam network. A new simulation is then performed on the resulting 'damaged beam network' which is the undamaged beam network without the first damaged element. The process is repeated to identify the next damaged element. We iterate this process and stop the damage analysis when either the percolation network is disrupted or the in-plane stiffness drops below 1% of the undamaged value. We identify either of these occurrences as 'mechanically induced network failure'.

To evaluate the effect of mechanical damage on the electrical response of the network, a recursive approach is employed. The electrical simulations start with an undamaged beam network. Subsequently, one damaged element is excluded from the simulations at a time. This procedure enables a direct comparison between the evolution of electrical and mechanical properties for the same portion of damaged network.

Several authors [6–10,27] agree that stress accumulates in sections of NWs near junctions due to constraints from neighboring NWs, thereby making these regions susceptible to failure. This failure mechanism is consistent with our modeling approach, as explained in section S4 of Appendix A. However, it is important to note that the failure in metal NWs is intricately linked to factors such as the crystallographic structure and the presence of defects like grain boundaries. These defects can serve as sites for stress/strain localization, ultimately leading to fracture or triggering the nucleation and transmission of dislocations [12,13,22–24,26,52]. These phenomena have not been included in our study.

2.2. Electrical damage characterization

The percolation network is converted into an equivalent resistor network to determine the in-plane effective conductivity κ_{eff} of the NW electrode and to conduct the electrical damage analysis. Since the approach described in Ref. [14] is replicated in this study, only a short summary of the numerical simulation procedure is provided in section S5 of Appendix A.

We simulate the in-plane electric conduction process and evaluate the effective conductivity κ_{eff} as

$$\kappa_{\mathrm{eff}} = \frac{I}{\Delta V\, t}, \tag{3}$$

which is understood as the property that relates the potential difference ΔV across the domain to the electric current I flowing through it. At variance with Ref. [14], the thickness t of the electrode is introduced in the definition of the effective conductivity for consistency with the mechanical simulations (refer to Section 2.1 and section S4 of Appendix A).

The procedure pursued for the electrical damage evolution analysis is similar to the mechanical one. The electrical conduction process is first simulated on the 'undamaged resistor network'. The element associated with the maximum value of current is identified and removed from the network. The procedure is recursively repeated until the removal of the damaged element causes the complete degradation of the percolation network. Since the electrical conduction process is halted if a percolation network no longer exists, we identify the 'electrically induced network failure' with this occurrence. The simulation strategy employed for analyzing electrical damage is comparable to the method proposed by Charvin et al. [32] for characterizing the degradation of metallic NW networks caused by localized Joule heating. This approach has been demonstrated to replicate experimental observations.

To assess the impact of the electrical damage on the network mechanical behavior, a series of mechanical simulations is conducted, mirroring the methodology used for the mechanical response. The simulations begin with the beam network corresponding to the pristine resistor network, and are iteratively repeated by removing one damaged element at a time.

3. Macroscopic electrode response: Parametric investigation

We aim to provide an overview of the dependence of the macroscopic mechanical electrode response on electrode design parameters. To this end, we investigate the dependence of the in-plane effective stiffness on three parameters: NW content n, NW cross-sectional shape, and flexural stiffness of the junction. Table S1 of Appendix A lists lower and upper bound values for the parameters under investigation, while details regarding their identification is provided next.

NW content. The macroscopic response of metal NW electrodes shows a percolative behavior and strongly depends on the NW content. The percolation threshold (expressed in terms of density (1)) of a two-dimensional random assembly of widthless one-dimensional objects is $n_{\mathrm{c}} \approx 5.64$ [57]. We therefore examine the response of observable geometries with NW content in a range between $n = 6$ and 60, which approximately corresponds to a range from $n = n_{\mathrm{c}}$ to $10n_{\mathrm{c}}$. This interval of values includes the range of values appealing for AgNWs transparent electrode applications (between $5n_{\mathrm{c}}$ and $10n_{\mathrm{c}}$ according to Bellet et al. [4]) and conforms to the range of values considered in several numerical investigations (up to $4n_{\mathrm{c}}$ in Ref. [42], up to $7n_{\mathrm{c}}$ in Ref. [14], and up to $10n_{\mathrm{c}}$ in Ref. [37]).

NW cross-sectional shape. The in-plane effective stiffness of the network is influenced by various factors, with the axial and flexural response of the NWs being among the most important. An important factor is the shape of the NW cross section [23,45] as shown next. Indicating with E_w the Young's modulus, A_w the cross-sectional area, and I_w the moment of inertia of the NWs, the ratio between axial $E_w A_w$ and flexural $E_w I_w$ rigidity is A_w/I_w. The value of this ratio depends only on the shape of the NW cross section, which ranges from approximately circular to polygonal depending on the synthesis process and the characteristic size of the NWs. For example, NWs synthesized by the polyol method exhibit a characteristic pentagonal cross-section [44] when the diameter is greater than about 120 nm; when the diameter is smaller than about 100 nm [45], the shape appears rounded. In contrast, NWs synthesized by physical vapor deposition show a truncated rhombic shape [24]. As a consequence, several cross-sectional shapes have been experimentally studied (circular [45], pentagonal [8–10,12,13,20–23,25,26,41,45,46], truncated rhombic [24]) and considered in numerical investigations (pentagonal [52,58], rhombic [58], truncated rhombic [58], circular [59]).

In this parametric investigation, the dependence of the NW cross-sectional shape is accounted for implicitly through the axial–flexural contribution defined by the non-dimensional parameter

$$\beta_{af} = \frac{A_w^2}{I_w}. \tag{4}$$

A higher value of β_{af} implies a greater dominance of the axial response over the flexural response. Furthermore, the value of β_{af} increases monotonically with the number of edges of regular-polygon-shaped cross sections. We conduct numerical simulations using both square and circular cross sections, and therefore β_{af} ranges from 12 to $4\pi = 12.566$ (Table S1 of Appendix A). The entire range of parametric investigations is carried out using a constant value for the reference diameter d_c, whose value is provided in Table S1.

The in-plane effective stiffness of the network is also influenced by the shear deformation, which depends on various factors at the NW level such as the cross-sectional shape, length, and stiffness, as detailed in section S3 of Appendix A. In that section, we provide a justification for utilizing the Timoshenko beam theory to accurately account for shear deformation.

Flexural stiffness of the junction. The mechanical and electrical network responses are ultimately determined by the properties of the NWs and their junctions. Numerous studies show that the NW-to-junction electrical resistance ratio is crucial for the electrical response of NW networks (refer, for example, to Refs. [14,32,37–39]). It will be shown in the following that, in analogy to the electrical network response, the mechanical network response is influenced by the mechanical properties of both the NWs and the junctions, and the relationship between them.

From the mechanical perspective, the junction can be characterized in terms of its capability to oppose to relative rotations and sliding between NWs. Two parameters, flexural (denoted by k_f) and translational stiffness, can therefore be introduced. According to experimental observations, the welding process determines the extent of the relative rotations between welded NWs. Hwang et al. [6,7], for example, show that junctions obtained with a thermal annealing process are bulkier than those obtained with mechanical welding, ultimately resulting in lower degree of flexibility and higher stress concentration in the proximity of the junction. While relative rotations between welded NWs are expected to take place, relative sliding is unlikely to occur unless the junction is damaged. A comprehensive understanding of damage evolution at the junction would require lower scale analyses (*e.g.*, performing atomistic simulations). This task, however, falls beyond the scope of the current study and we therefore restrict our analyses to the relative rotation case only. Driven by similar considerations, Wang et al. [34,35] performed numerical simulations focusing on the role of the flexural stiffness at the fiber junction ('fiber–fiber bonds' in the references).

We introduce a simple junction model in which we assume that the junction provides a perfect constraint for the relative displacements of NWs (*i.e.*, they are impeded) but allows relative rotations to take place. The mathematical details are provided in section S4 of Appendix A. For a rigid-joint junction, k_f tends towards infinity, indicating that the relative rotation between NWs is impeded. For a pin-joint junction, k_f tends towards zero, indicating that relative rotations between NWs are allowed. In the current investigation, we exclusively consider the two limit cases $k_f \to \infty$ and $k_f \to 0$ accordingly. Expressing k_f in terms of the flexural stiffness of the NW segments, conditions $k_f \to \infty$ and $k_f \to 0$ correspond to the cases $k_f \gg E_w I_w/d_c$ and $k_f \ll E_w I_w/l_w$, respectively.

4. Results

We present a summary of the findings from the numerical simulations. To provide a contextual framework for the results, the analysis of the network response at different NW contents is described first, followed by the study of the network damage. The number of realizations employed to conduct the investigations is specified in each section and refers to the number of percolated networks considered (more realization are generated at $n = n_c$ to obtain the same number of percolated networks). Material and geometrical parameters employed in the numerical simulations are listed in Table S1 of Appendix A.

4.1. Macroscopic electrode response

Figs. 2a and b depict the correlation between the in-plane stiffness E_{eff} (2) and the NW content n. Three scenarios are examined, each involving a different combination of NW cross sections and mechanical behavior of the junctions: A) square cross section with rigid-joint junctions ($k_f \to \infty$), B) circular cross section with pin-joint junctions ($k_f \to 0$), and C) circular cross section NWs with rigid-joint junctions ($k_f \to \infty$). The markers in the plots correspond to the average in-plane effective stiffness (2), which was determined from 100 numerical realizations for each NW content. Numerical simulations are performed according to the procedure described in Section 2.1.

Fig. 2a shows that there is a significant variation in the value of E_{eff} over the range of NW content from n_c to $10n_c$, encompassing a range of five to six orders of magnitude. The dependence on the specific combination of cross section and junction flexural stiffness is rather small and becomes negligible at large n. Based on the slope of the curves, two distinct regions can be identified. Between the percolation threshold n_c and four times the percolation threshold, the in-plane effective stiffness E_{eff} increases by more than four orders of magnitude, ranging from approximately 2 kPa to around 700 MPa, depending on the considered combination of cross section and junction flexural stiffness. However, over the range of four to ten times the percolation threshold, the change in E_{eff} is at most one order of magnitude, increasing from about 700 MPa to around 8 GPa. As the NW content n approaches $10n_c$, the curves show a reduced slope, and at $n = 10n_c$, they approach $E_{eff} = 8$ GPa, which is more than an order of magnitude lower than E_w. The strong dependence of the effective stiffness on the NW content within the range n_c to $4n_c$ can be attributed to the percolative behavior of the system.

Combination A produces the highest effective stiffness over the entire range of NW content, while combination B produces the lowest. Fig. 2b displays the relative difference

$$\Delta E_{eff} = \frac{|E_{eff,ref} - E_{eff,i}|}{E_{eff,ref}}$$

between different combinations of cross section and junction mechanical responses. In the expression above, $E_{eff,ref}$ and $E_{eff,i}$ are the values of the effective stiffness E_{eff} (shown in Fig. 2a) at a given NW content

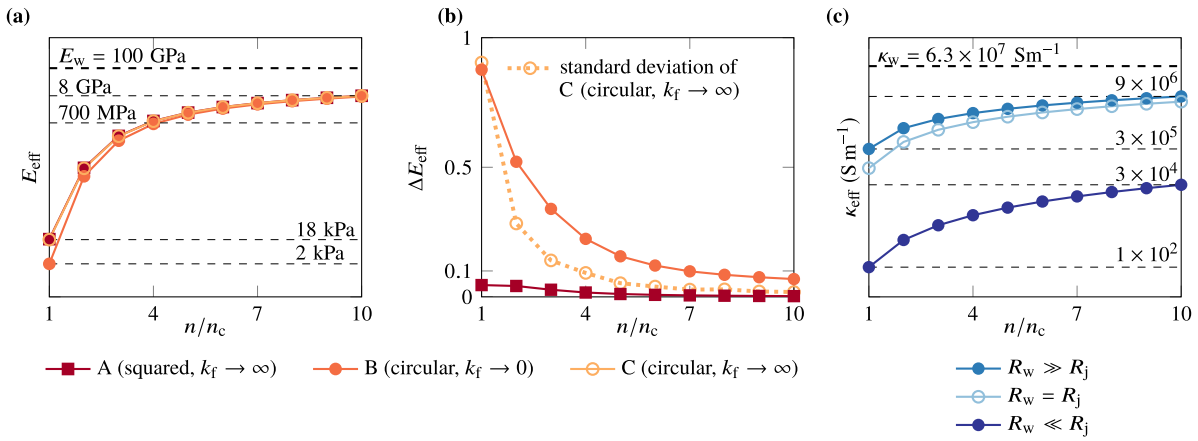

Fig. 2. Dependence of network effective properties on NW content n (results obtained with the material parameters listed in Table S1 of Appendix A). (a) Effective stiffness (2) versus n for three combinations of NW cross-sectional shape (circular and square) and flexural stiffness of the junction (rigid-joint: $k_f \to \infty$, or pin-joint: $k_f \to 0$). Each marker represents the average of 100 realizations. (b) Relative difference ΔE_{eff} between the values of E_{eff} shown in panel (a). The combination of circular cross section NW and rigid-joint junctions ($k_f \to \infty$) is selected as the reference. The standard deviation of the values of E_{eff} for the combination of circular cross section NW and rigid-joint junctions is included for completeness. The values of the standard deviation are scaled by the average value of E_{eff} at the same NW content. (c) Effective conductivity (3) versus n for circular cross section NWs in the limit cases $R_w \gg R_j$, $R_w = R_j$, and $R_w \ll R_j$. The effective conductivity is computed as $\kappa_{eff} = 1/(R_S d_c)$, where R_S is the sheet resistance determined through the analytical equation proposed by Forró et al. [39]. The values of the NW properties E_w and κ_w are indicated in the plots.

for the reference combination and the combination being assessed, respectively. In this case, we select combination C (circular cross section and rigid-joint junctions) as the reference, and evaluate combinations A and B relative to it.

The standard deviation of the values of E_{eff} computed with combination C is displayed for reference in Fig. 2b (empty circle symbols and yellow line). The values are scaled by the average values of E_{eff} shown in Fig. 2a. We do not report the standard deviation of combinations A and B because differences with the values reported are visible only at $n = n_c$, while all the curves overlap for $n \geq 2n_c$. As the NW content approaches the percolation threshold n_c, the standard deviation increases, which is expected as it is known that at $n = n_c$ the effective properties show a large degree of variability.

Fig. 2b shows that the relative difference ΔE_{eff} monotonically reduces with n and reaches a value below 7% at $n = 10n_c$ for both combinations A and B. The comparison between combination A and C (square purple symbols in Fig. 2b) shows that the effect of the shape of the cross section is modest and barely sensitive to n. The extent of the relative difference is 4%, lower than the standard deviation. The comparison between combinations B and C (full orange circle symbols in Fig. 2b) shows that the impact of the junction flexural stiffness on the effective stiffness strongly depends on n and is significant at low NW contents. In fact, the value of ΔE_{eff} approaches 1 as n approaches n_c (at $n = n_c$ the effective stiffness of combinations B and C differ by an order of magnitude as shown in Fig. 2a). Intuitively, the network becomes more entangled as the NW content increases. Indeed, the average number of junctions per NW is linearly proportional to n while the average segment length scales as $1/n$ [55], thus rendering the junction flexibility k_f less critical to the effective mechanical stiffness. From these observations, we draw three main conclusions. First, the NW content is the key design factor: when the NW content reaches sufficiently high values the influence of the cross section shape and junction flexural stiffness on the effective stiffness vanishes. Second, when modeling the mechanical response of the network, assuming that NWs have circular cross section is an acceptable approximation irrespective of the NW content. Third, accurately characterizing the mechanical properties of the junction is crucial for predicting the mechanical properties of the network at small n. This aspect is particularly relevant for applications where high transparency requirements limit the amount of NWs that can be used.

Fig. 2c shows the dependence of the effective conductivity κ_{eff} (3) on the NW content for the limit cases $R_w \gg R_j$, $R_w = R_j$, and $R_w \ll R_j$. The values of the effective conductivity are computed using the analytical expression proposed by Forró [39] (a comparison between this analytical expression and our computational strategy for the evaluation of the effective conductivity is available in Ref. [14]). The general pattern observed in the effective conductivity is similar to that of the effective stiffness. There are however two notable differences. First, the range of values spanned by κ_{eff} is much narrower, around two orders of magnitude, compared to that of E_{eff}. Second, the ratio between nanowire and junction resistances (R_w/R_j) has a more significant effect on the effective conductivity than the junction flexibility (k_f) has on the effective stiffness. In fact, the curve corresponding to $R_w \gg R_j$ is shifted three orders of magnitude higher than the curve corresponding to $R_w \ll R_j$. An intrinsic difference between the electrical and mechanical model formulations clearly emerges here. Since the electric potential is a scalar field, the electrical response of the junction is completely described by the junction resistance R_j, and condition $R_w \ll R_j$ represents a weak electrical connection between the NWs. The displacement field is vectorial instead. The flexural stiffness k_f therefore provides a partial description of the mechanical response of the junction. As we assumed that no sliding between NWs take place (translational stiffness approaching infinity), the condition $k_f \to 0$ represents a weak mechanical connection in terms of relative rotations only, being the relative sliding between NWs prevented.

4.2. Damage assessment

We proceed with the identification of the correlation between the extent of the local network damage and the macroscopic network response. Since the results just discussed show that the shape of the cross section has a minor impact on the mechanical response of the network, we consider NW with circular cross section only. We also restrict the investigation to the junction setting that provides the best mechanical and electrical response: such a setting corresponds to the limit of infinite flexural stiffness ($k_f \to \infty$) and negligible junction resistance ($R_w \gg R_j$).

We quantify the extent of the local network damage through the number of damaged elements N_d and damage ratio

$$d_m = \frac{l_d}{l_t}, \tag{5}$$

where $l_d = \sum_{i=1}^{N_d} l_{d,i}$ is the cumulative length of the damaged NW segments, $l_t = l_w N_w$ is the sum of the length of the sticks in the realization,

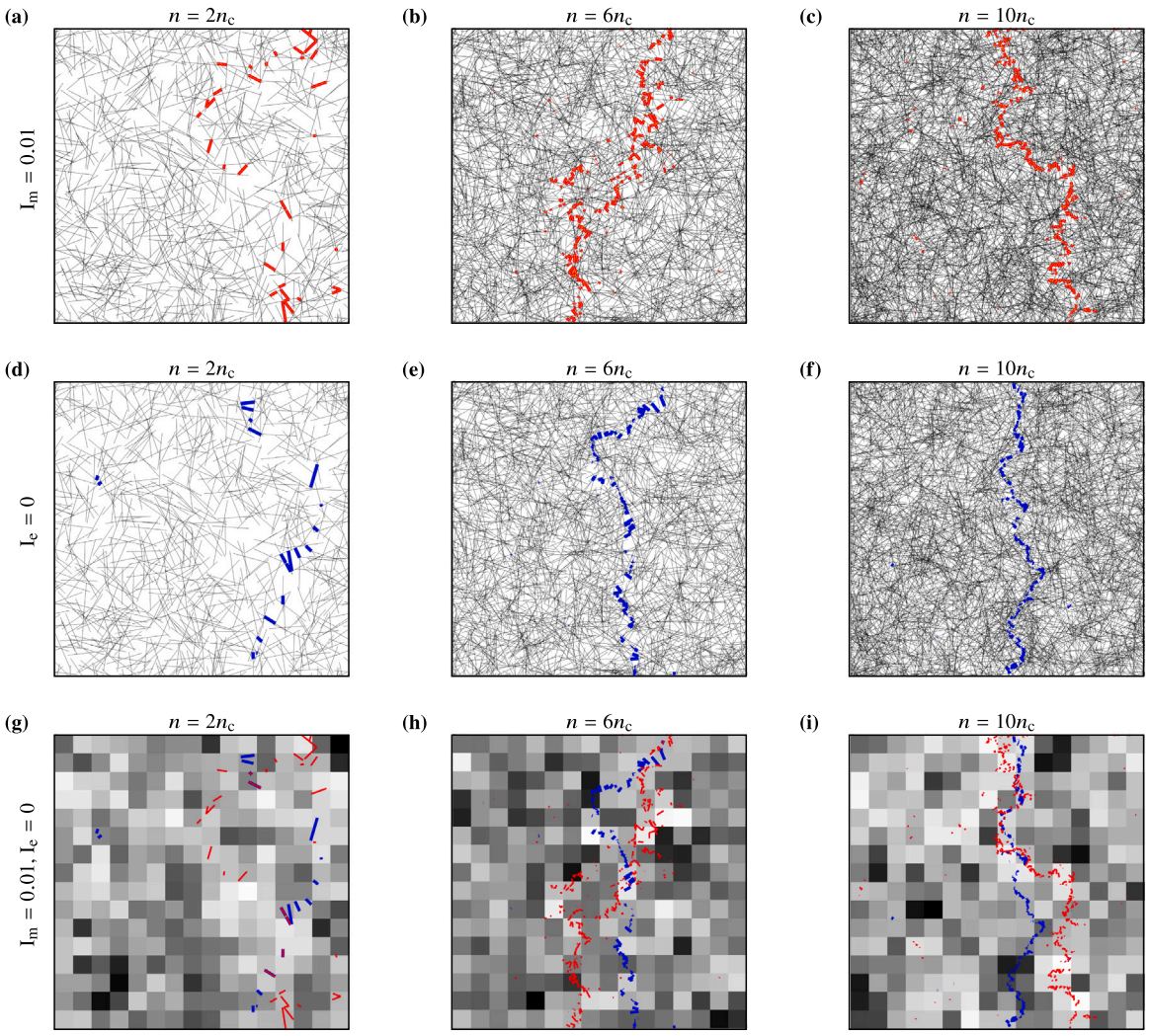

Fig. 3. Damaged element pattern. (a–c) Damaged elements at failure ($I_m = 0.01$) identified through the numerical simulation of the mechanical damage evolution process. Results for three realizations at $n = 2n_c$ (a), $n = 6n_c$ (b), and $n = 10n_c$ (c). Damaged and intact elements are highlighted in red and black, respectively. (d–f) Damaged elements at failure ($I_e = 0$) identified through numerical simulations of the electrical damage evolution process. The same realizations represented in panels (a–c) are considered. Damaged and intact elements are highlighted in blue and black, respectively. (g–i) Local NW density maps for the realizations shown in panels (a–f). A regular grid of squares with edge size $l_q = L/16$ is employed for the discretization. Darker squares indicate higher density. Damaged elements identified through the numerical simulations of mechanical (red) and electrical (blue) damage evolution processes are superimposed to the maps.

and $l_{d,i}$ is the length of the i-th damaged segment. We assess the macroscopic network response in terms of mechanical and electrical integrity defined as

$$I_m = \frac{E_{eff,dd}}{E_{eff,ud}}, \quad \text{and} \quad I_e = \frac{\kappa_{eff,dd}}{\kappa_{eff,ud}}, \tag{6}$$

respectively. In the expression above, the subscripts dd and ud make reference to a property being evaluated in the damaged and undamaged network, respectively. According to our numerical simulation setting, the integrity I_e is constrained to the range between 0 (corresponding to the network failure) and 1 (representing an undamaged network), while I_m is constrained to the range between 0.01 and 1 (refer to Section 2.1 for details).

The identification of mechanically damaged elements is performed according to the procedure described in Section 2.1. In the search of the highest mechanical stress we exclude the vertical strips near the vertical edges. These two strips extend from the bottom to the top of the simulation domain and are $0.025L$ wide (the excluded domain therefore amounts to 5% of the entire domain). The exclusion of these regions is necessary because stress tends to localize along the vertical edges due to the enforcement of boundary conditions. These localizations can be misleading and do not provide a representative picture of the overall electrode response.

Fig. 3 shows examples of the spatial distribution of damaged elements throughout the network. Numerical simulations are carried out to investigate the mechanical (Fig. 3a–c) and electrical (Fig. 3 d–f) damage processes. Examples of spatial distribution of damaged elements at mechanical failure ($I_m = 0.01$) for three realizations at $n = 2n_c$ (a), $n = 6n_c$ (b), and $n = 10n_c$ (c) are shown in Figs. 3a–c. The spatial distributions of damaged elements at electrical failure ($I_e = 0$), for the same realizations, are shown in Figs. 3d–f. Crack-like patterns are recognizable regardless of the physical process driving the damage, whether it is mechanical or electrical, with fully-developed cracks at failure splitting the network in two disconnected regions. The crack patterns in Fig. 3 are consistent with those observable in the experimental post failure scanning electron microscopy (SEM) images of AgNW [18,19] and carbon nanotube [40] networks, in which electrical failure was induced. Similar patterns result also from the numerical simulations of Charvin et al. [32], who pursued the approach described in Section 2.2. Fig. 3 shows also that mechanical and electrical damage analyses performed on the same realization result in different sets of damaged elements (compare a–c against d–f). This stems from the observation that mechanical and electrical stresses reach their maximum

values at distinct locations within the same network (refer to the maps shown in Fig. 1c for an example). The mechanical damage evolution process from $I_m = 1$ to 0.01 involves a larger number of damaged elements compared to the electrical one (more details are provided in the following paragraphs). Overall, the spatial distribution of damaged elements resulting from the mechanical damage analyses (a–c) appears more dispersed compared to those resulting from the electrical damage analyses (d–f), irrespective of the NW content.

Metal NW networks can also be coated with an oxide layer [15,27,31] or embedded in a polymeric matrix [29,30] to enhance stretchability or to achieve application-tailored performance improvements. Experimental investigations show that, when subject to mechanical loads capable of inducing NW failure, macroscopic cracks progressively develop [15,27,31,33] and that a concurrent increase of the sheet resistance is detected. Despite these analogies with coating-free NW network, the crack initiation and propagation process of these system is more complex. This complexity arises from both the mutual interactions among NWs and, especially, on the interplays between the NWs and the surrounding material. More appropriate simulations strategies are therefore needed. For example, the mechanical behavior of ensembles of one-dimensional inclusions in a hosting matrix is often performed by means of numerical approaches that rely on embedded fiber models [60]. These approaches have recently been modified to simulate electrochemical processes taking place in fibrous electrodes for rechargeable batteries [61] and appear thus appropriate to investigate the electrical-mechanical response of transparent electrodes at once.

Figs. 3g–i show the local NW density maps obtained from the observable geometries shown in Figs. 3a–f. The construction of NW density maps starts from the discretization of the simulation domain with a grid of squares of equal size l_q. The NW density in each square of the grid is computed as the sum of the length of the NW segments within the square divided by l_q^2. The spatial distributions of damaged elements shown in Figs. 3a–f are superimposed to the NW density maps. Figs. 3g–i show that there is no obvious correlation between the local NW density and the location of the damaged elements, as they appear to be equally located in high (dark) and low (bright) density squares. Repeating the analysis using larger or smaller grid discretizations (not shown for brevity) did not lead to any significant differences, and no clear trend emerged. The results of this preliminary analysis suggest that relying solely on a visual inspection of NW electrode micrographs is not a reliable approach for predicting the location of damage. Therefore, it appears necessary to carry out analyses of the mechanical and electrical network responses, as described next.

4.3. Mechanical damage analysis

Figs. 4a–d summarize the results of the mechanical damage simulations. The evolution of damage is tracked from the undamaged stage ($I_m = 1$) up to failure ($I_m = 0.01$). The effective conductivity is assessed at a later stage by repeating electrical numerical simulations on the network that has undergone mechanical damage.

Figs. 4a and b illustrate the correlations between mechanical integrity I_m, electrical integrity I_e, and the number of mechanically-damaged elements for ten realizations with n ranging from n_c to $10n_c$. The effective stiffness $E_{eff,ud}$ and conductivity $\kappa_{eff,ud}$ values of the undamaged networks are consistent with the average values in Fig. 2 at the corresponding NW content, and these values are used to calculate I_m and I_e using (6).

The curves describing the dependence of I_m and I_e on N_d show clear distinguishing features. The relationship between I_e and N_d (full symbols) is only linear for a portion of the damage evolution process, while the mechanical integrity I_m (empty symbols) exhibits an approximately linear dependence on N_d over the entire range from $I_m = 1$ to 0.01. As N_d approaches the value corresponding to the mechanical failure ($I_m = 0.01$), the electrical integrity I_e shows an abrupt decrease. Interestingly, Figs. 4a, b show that mechanical damage compromises the electrical performance only partially. In fact, all the curves representing I_e lie above the corresponding curve representing I_m, with $I_e \approx 0.5$ when mechanical failure ($I_m = 0.01$) is attained. We therefore conclude that the 'flow' of stresses (resulting from the mechanical equilibrium) and the flow of electric current (resulting from charge conservation) follow different paths within the network. As a consequence, an electric conduction pattern through the network still exists when the effective stiffness of the network amounts to 1% of the undamaged value ($I_m = 0.01$). This observation indicates that even with the presence of a considerable number of mechanically-damaged elements, the networks still maintain a relatively high level of effective conductivity, which is about 50% of the undamaged effective conductivity $\kappa_{eff,ud}$. This trend is independent of the NW content.

Figs. 4a and b also show that the number of damaged element at failure is directly proportional to n, thus confirming the conclusion that can be drawn from the visual inspection of Fig. 3: as the NW content increases, the network becomes more entangled, requiring a larger number of NW failures to split it into disconnected subsets. To validate this statement, the relationship between N_d and n is shown in Fig. 4d. Five realizations are considered for each NW content. The average values are displayed in the plot. We emphasize that mechanical failure is attained at $N_d = 1$ with the realizations at $n = n_c$. We therefore conclude that the breakdown of a few elements (a single element in the worst case scenario) is sufficient to cause the failure of the NW network if the NW content approaches the percolation threshold.

Fig. 4c presents an alternative representation of the relationship between the macroscopic network response and the local network damage. Instead of using the number of damaged elements N_d, damage is expressed in terms of d_m (5). The curves for mechanical integrity I_m shown in Figs. 4a and b are compressed into a narrow range of values. At failure, d_m ranges from 6×10^{-3} to 1.2×10^{-2}. The curves almost overlap, suggesting that roughly the same percentage of network (expressed in terms of length) is damaged at failure, regardless of the NW content.

4.4. Electrical damage analysis

Figs. 4e–h summarize the results of the electrical damage simulations. The procedure is specular to the procedure that led to the results shown in Figs. 4a–d. The electrical numerical simulations are performed first, and the effective stiffness is assessed afterwards. The damage evolution is tracked from the undamaged stage ($I_e = 1$) up to failure ($I_e = 0$). The results in Figs. 4e–h were obtained using the same realizations as those used to generate the results in Figs. 4a–d.

Figs. 4e and f show the relationships between electrical I_e and mechanical I_m integrity and the number of electrically damaged elements. The curves representing the relationship between I_e and N_d (full symbols) show an approximately linear trend (up to $I_e \approx 0.2$) with a sudden drop in close proximity of electrical failure. This response is consistent with the result reported by Charvin et al. [32] who investigated the behavior of the sheet resistance R_S (which is equivalent to $R_S = 1/(\kappa_{eff}\, d_c)$, with κ_{eff} defined according to (3) and $t = d_c$) as a function of the number of simulation steps (equivalent to N_d). They show that the dependence is approximately linear for a significant portion of the simulation (around 110 steps out of 140), but a rapid increase in R_S occurs during the remaining part of the simulation (see Figure 4 in the reference).

The electrical integrity curves shown in Figs. 4e, f are generally steeper than their counterparts in Figs. 4a, b. This is mainly due to the fact that the number of damaged elements N_d corresponding to the failure condition $I_e = 0$ is lower (roughly half) than that needed for the failure condition $I_m = 0.01$ for a given NW content. The comparison between the two sets of curves is obvious from Figs. 4d and 4h, where the maximum value of N_d is approximately 600 and 300, respectively.

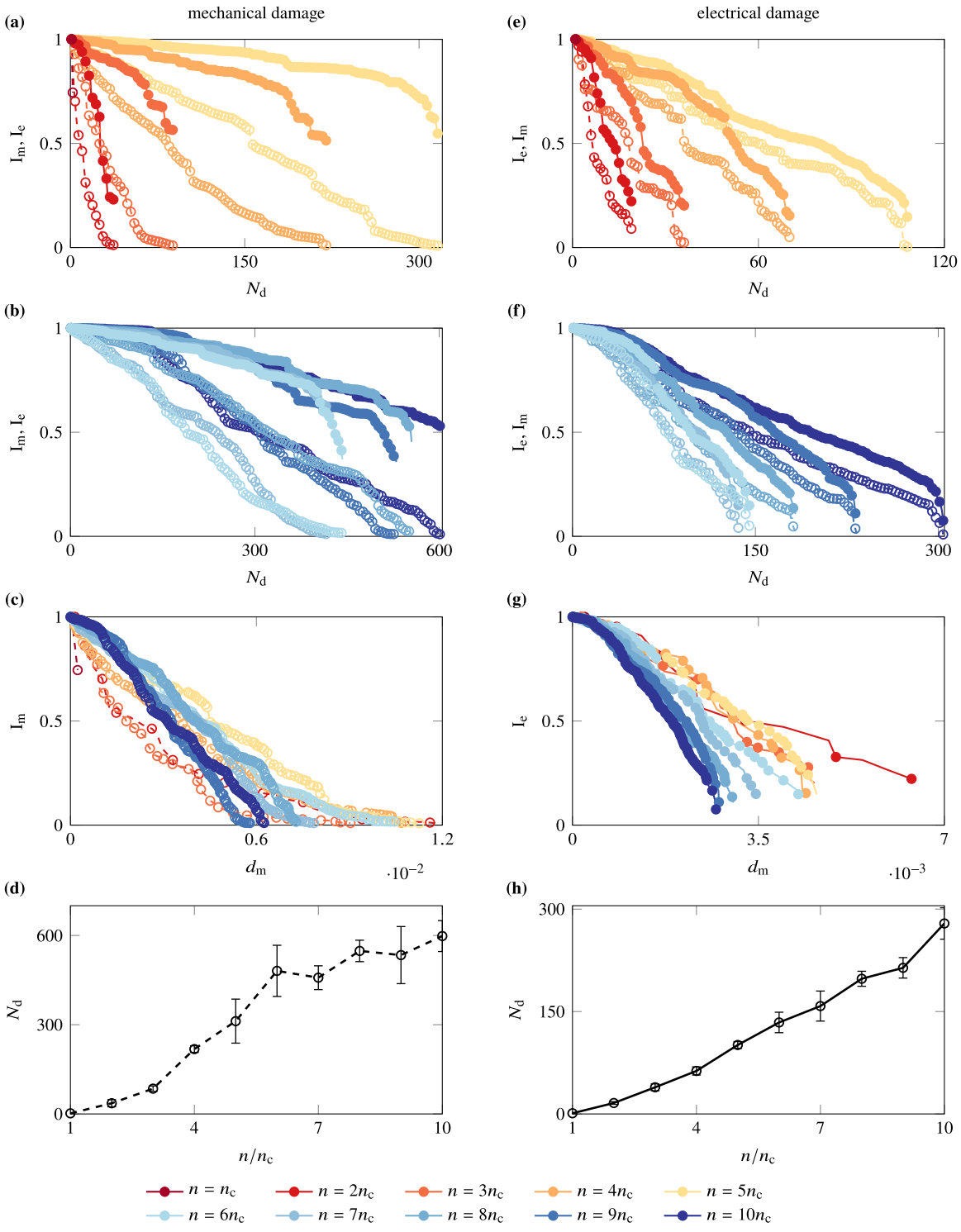

Fig. 4. Damage processes and impact on the network response. Mechanical I_m and electrical I_e integrity (6) are indicated with empty and full symbols, respectively. Consistently, the same color is employed to indicate identical content n in both cases. Mechanical (a–d) and electrical (e–h) damage. (a, b, e, f) Mechanical and electrical integrity dependence on the number of damaged elements N_d. Five realizations with NW content n in the range from n_c to $5n_c$ (a, e), and five in the range from $6n_c$ to $10n_c$ (b, f). (c) Mechanical integrity dependence on local network damage d_m (5) for the datasets considered in panels (a) and (b). (g) Electrical integrity dependence on local network damage d_m (5) for the datasets considered in panels (e) and (f). (d, h) Average number of damaged elements N_d versus NW content. Each marker represents the average value of five realizations, while the error bar expresses the standard deviation.

Remarkably, the curves representing the mechanical integrity I_m (empty symbols) in Figs. 4e, f are consistently lower than those representing electrical integrity I_e (for a given NW content). This observation may seem counterintuitive and requires some explanation. We recall that we use an electrical damage simulation that involves the iterative removal of the network element with the highest current value. This results in a more significant reduction in stiffness compared to effective conductivity (i.e., the reduction in I_m is more pronounced than in I_e). Consequently, the impact of the electrical damage is more detrimental for the mechanical response of the network than for the electrical response itself. We attribute this effect to the altered 'flow' of stresses through the network caused by the electrical damage. To estimate the

magnitude of this effect, one can compare the curves representing I_m in Figs. 4e, f with those in Figs. 4a, b. It is evident that the effect of electrical damage on effective stiffness is more detrimental than that of mechanical damage alone. This can be readily confirmed by comparing the values of I_m in those figures for the same n and N_d.

We can conclude that the element of the network subject to the highest stress level (according to the criterion described in Section 2.1) is not necessarily the most critical element for the network mechanical response. Therefore, the maximum electric current criterion is the most conservative alternative in identifying the most critical element for both electrical and mechanical responses.

Fig. 4g shows the relationship between electrical integrity and d_m. A more concise representation of the results is obtained compared to Figs. 4e, f, and it reveals a regular trend that differs from Fig. 4c: the value of d_m at failure progressively decreases with increasing n, ranging from 6.4×10^{-3} for $n = n_c$ to 2.7×10^{-3} for $n = 10n_c$.

5. Conclusions

The computational approach employed in this study is based on several key modeling simplifications. To begin with, the mechanical and electrical damage analyses are conducted independently without considering any coupling effects (their mutual influence is however addressed in a loosely coupled approach). Next, the damaged NW segments are assumed to undergo a sharp transition from fully operational to inactive. Finally, the electrical and mechanical responses of the NW are assumed to be linear throughout the analysis. These assumptions allow us to perform damage analyses through a recursive search for the most stressed (either mechanically or electrically) element of the NW network using a loop of linear analyses (see Sections 2.1 and 2.2).

Our investigation suggests that it is necessary to analyze both mechanical and electrical stresses within a network in order to identify damaged NWs, since a visual inspection of the electrode morphology cannot be conclusive (as discussed in Section 4.2). Our findings demonstrate that the spatial distributions of mechanical stresses and electric current within the network differ, as evidenced by Fig. 1c. This difference in turn influences the locations where stress and electric current are most intense. As damage initiation and propagation follow different paths depending on the physical phenomena that trigger them (as discussed in Section 4.2), both mechanical and electrical stress analyses are necessary for a comprehensive damage assessment. However, if only a single analysis can be conducted, priority should be given to the examination of electrical damage due to its more detrimental impact. Indeed, the results discussed in Sections 4.3 and 4.4 show that electrical damage causes the most severe reduction of mechanical and electrical functionalities of the electrode, irrespective of the NW content.

It is important to note that the modeling simplifications utilized in this study may affect the accuracy and predictability of the model. Neglecting coupling effects may lead to erroneous estimate of the damage level and, consequently, of the failure load. Bending of a single NW, for example, has been demonstrated to provide a mitigation strategy against electromigration breakdown [12]. The assumption of a sharp transition from fully operational to inactive may not accurately depict the actual behavior of the material, which could potentially undergo a gradual deterioration prior to reaching failure. Most importantly we could not meaningfully compare the critical quantities that lead to failure by means of the two mechanisms: we have assumed that the applied load is large enough to break the component with max stress and that the potential leads to failure of the component with largest current. This does not mean to be.

The assumption of linear behavior may be valid only for small deformations and low current densities, while the actual response may be nonlinear for large deformations and high current densities. Additionally, including non-linear effects such as plastic deformation or non-ohmic electrical response would result in a distinct evolution of the damage pattern that could generate correlations between local damage and electrical and mechanical functionality that are different from those demonstrated in Sections 4.3 and 4.4. Finally, due to the linear response assumption and the peak value criterion adopted in our damage analyses, the results are not affected by the magnitude of the deformation or the applied potential difference. This insensitivity implies that the model does not consider scenarios where multiple NWs exceed their yield stress during a single iteration of the mechanical damage analysis. Further investigations are needed to assess the validity of these simplifications and to improve the accuracy and reliability of the model.

CRediT authorship contribution statement

Davide Grazioli: Conceptualization, Data curation, Formal analysis, Investigation, Methodology, Project administration, Software, Supervision, Validation, Visualization, Writing – original draft, Writing – review & editing. **Gabriele Gangi:** Formal analysis, Investigation, Software, Writing – review & editing. **Lucia Nicola:** Investigation, Writing – review & editing. **Angelo Simone:** Funding acquisition, Resources, Investigation, Supervision, Writing – review & editing.

Declaration of competing interest

The authors declare that they have no known competing financial interests or personal relationships that could have appeared to influence the work reported in this paper.

Data availability

Data will be made available on request.

Acknowledgments

A.S. acknowledges funding from the Department of Industrial Engineering at the University of Padova for the project *Computational multiscale and multiphysics modeling of mechanically induced failure in fibrous metal transparent flexible electrodes* (Finanziamento SID 2022). L.N. acknowledges funding from the European Research Council (ERC) under the European Union's Horizon 2020 research and innovation programme (grant agreement no. 681813).

Appendix A. Supplementary data

Supplementary material related to this article can be found online at https://doi.org/10.1016/j.compscitech.2023.110304.

References

[1] J.J. Patil, W.H. Chae, A. Trebach, K.-J. Carter, E. Lee, T. Sannicolo, J.C. Grossman, Failing forward: Stability of transparent electrodes based on metal nanowire networks, Adv. Mater. 33 (5) (2020) http://dx.doi.org/10.1002/adma.202004356.

[2] D.T. Papanastasiou, A. Schultheiss, D. Muñoz-Rojas, C. Celle, A. Carella, J.-P. Simonato, D. Bellet, Transparent heaters: A review, Adv. Funct. Mater. 30 (21) (2020) http://dx.doi.org/10.1002/adfm.201910225.

[3] Y. Ding, Y. Cui, X. Liu, G. Liu, F. Shan, Welded silver nanowire networks as high-performance transparent conductive electrodes: Welding techniques and device applications, Appl. Mater. Today 20 (2020) http://dx.doi.org/10.1016/j.apmt.2020.100634.

[4] D. Bellet, M. Lagrange, T. Sannicolo, S. Aghazadehchors, V. Nguyen, D. Langley, D. Muñoz-Rojas, C. Jiménez, Y. Bréchet, N. Nguyen, Transparent electrodes based on silver nanowire networks: From physical considerations towards device integration, Materials 10 (6) (2017) http://dx.doi.org/10.3390/ma10060570.

[5] D. Stauffer, A. Aharony, Introduction to Percolation Theory, Taylor & Francis, 2018, http://dx.doi.org/10.1201/9781315274386.

[6] B. Hwang, H.-A.-S. Shin, T. Kim, Y.-C. Joo, S.M. Han, Highly reliable Ag nanowire flexible transparent electrode with mechanically welded junctions, Small 10 (16) (2014) http://dx.doi.org/10.1002/smll.201303906.

[7] B. Hwang, T. Kim, S.M. Han, Compression and tension bending fatigue behavior of Ag nanowire network, Extreme Mech. Lett. 8 (2016) http://dx.doi.org/10.1016/j.eml.2016.02.011.

[8] B. Hwang, J.G. Seol, C.-H. An, S.H. Kim, Bending fatigue behavior of silver nanowire networks with different densities, Thin Solid Films 625 (2017) http://dx.doi.org/10.1016/j.tsf.2017.01.048.

[9] M.-J. Kim, D.-S. Ko, J.-H. Kim, E.-H. Cho, D.J. Yang, C. Kwak, H. Sohn, Silver nanowires network film with enhanced crystallinity toward mechano-electrically sustainable flexible-electrode, Adv. Mater. Technol. 6 (1) (2020) http://dx.doi.org/10.1002/admt.202000838.

[10] N.J. Schrenker, Z. Xie, P. Schweizer, M. Moninger, F. Werner, N. Karpstein, M. Mačković, G.D. Spyropoulos, M. Göbelt, S. Christiansen, C.J. Brabec, E. Bitzek, E. Spiecker, Microscopic deformation modes and impact of network anisotropy on the mechanical and electrical performance of five-fold twinned silver nanowire electrodes, ACS Nano 15 (1) (2021) http://dx.doi.org/10.1021/acsnano.0c06480.

[11] J. Zhao, H. Sun, S. Dai, Y. Wang, J. Zhu, Electrical breakdown of nanowires, Nano Lett. 11 (11) (2011) http://dx.doi.org/10.1021/nl202160c.

[12] N.M. Batra, A. Syed, P.M.F.J. Costa, Current-induced restructuring in bent silver nanowires, Nanoscale 11 (8) (2019) http://dx.doi.org/10.1039/c8nr08551j.

[13] M. Waliullah, R.A. Bernal, Current density at failure of twinned silver nanowires, Nanotechnology 33 (30) (2022) http://dx.doi.org/10.1088/1361-6528/ac64af.

[14] D. Grazioli, A.C. Dadduzio, M. Roso, A. Simone, Quantitative electrical homogeneity assessment of nanowire transparent electrodes, Nanoscale 15 (14) (2023) http://dx.doi.org/10.1039/d2nr06564a.

[15] V.H. Nguyen, J. Resende, D.T. Papanastasiou, N. Fontanals, C. Jiménez, D. Muñoz-Rojas, D. Bellet, Low-cost fabrication of flexible transparent electrodes based on al doped ZnO and silver nanowire nanocomposites: Impact of the network density, Nanoscale 11 (25) (2019) http://dx.doi.org/10.1039/c9nr02664a.

[16] D.T. Papanastasiou, N. Charvin, J. Resende, V.H. Nguyen, A. Sekkat, D. Muñoz-Rojas, C. Jiménez, L. Flandin, D. Bellet, Effects of non-homogeneity and oxide coating on silver nanowire networks under electrical stress: Comparison between experiment and modeling, Nanotechnology 32 (44) (2021) http://dx.doi.org/10.1088/1361-6528/ac1632.

[17] H.H. Khaligh, I.A. Goldthorpe, Failure of silver nanowire transparent electrodes under current flow, Nanoscale Res. Lett. 8 (1) (2013) http://dx.doi.org/10.1186/1556-276x-8-235.

[18] T. Sannicolo, N. Charvin, L. Flandin, S. Kraus, D.T. Papanastasiou, C. Celle, J.-P. Simonato, D. Muñoz-Rojas, C. Jiménez, D. Bellet, Electrical mapping of silver nanowire networks: A versatile tool for imaging network homogeneity and degradation dynamics during failure, ACS Nano 12 (5) (2018) http://dx.doi.org/10.1021/acsnano.8b01242.

[19] Y. Zhu, T. Wan, P. Guan, Y. Wang, T. Wu, Z. Han, G. Tang, D. Chu, Improving thermal and electrical stability of silver nanowire network electrodes through integrating graphene oxide intermediate layers, J. Colloid Interface Sci. 566 (2020) http://dx.doi.org/10.1016/j.jcis.2020.01.111.

[20] B. Wu, A. Heidelberg, J.J. Boland, J.E. Sader, Sun, Li, Microstructure-hardened silver nanowires, Nano Lett. 6 (3) (2006) http://dx.doi.org/10.1021/nl052427f.

[21] Y. Zhu, Q. Qin, F. Xu, F. Fan, Y. Ding, T. Zhang, B.J. Wiley, Z.L. Wang, Size effects on elasticity, yielding, and fracture of silver nanowires: *In situ* experiments, Phys. Rev. B 85 (4) (2012) http://dx.doi.org/10.1103/physrevb.85.045443.

[22] T. Filleter, S. Ryu, K. Kang, J. Yin, R.A. Bernal, K. Sohn, S. Li, J. Huang, W. Cai, H.D. Espinosa, Nucleation-controlled distributed plasticity in penta-twinned silver nanowires, Small 8 (19) (2012) http://dx.doi.org/10.1002/smll.201200522.

[23] S. Vlassov, B. Polyakov, L.M. Dorogin, M. Antsov, M. Mets, M. Umalas, R. Saar, R. Lõhmus, I. Kink, Elasticity and yield strength of pentagonal silver nanowires: In situ bending tests, Mater. Chem. Phys. 143 (3) (2014) http://dx.doi.org/10.1016/j.matchemphys.2013.10.042.

[24] S. Yin, G. Cheng, G. Richter, H. Gao, Y. Zhu, Transition of deformation mechanisms in single-crystalline metallic nanowires, ACS Nano 13 (8) (2019) http://dx.doi.org/10.1021/acsnano.9b03311.

[25] F.R. Poblete, Z. Cui, Y. Liu, Y. Zhu, Stretching nanowires on a stretchable substrate: A method towards facile fracture testing and elastic strain engineering, Extreme Mech. Lett. 41 (2020) http://dx.doi.org/10.1016/j.eml.2020.101035.

[26] B. Ojeda, M. Waliullah, A.-M.A. Hossain, T. Nguyen, T. Wettstein, Y. Tadesse, R.A. Bernal, High-throughput tensile testing of silver nanowires, Extreme Mech. Lett. 57 (2022) http://dx.doi.org/10.1016/j.eml.2022.101896.

[27] C. Lee, H. Kim, B. Hwang, Fracture behavior of metal oxide/silver nanowire composite electrodes under cyclic bending, J. Alloys Compd. 773 (2019) http://dx.doi.org/10.1016/j.jallcom.2018.09.212.

[28] C. Liu, C.A. Ainsworth, W.W. Sampson, B. Derby, Fatigue and the electrical resistance of silver nanowire networks, Scr. Mater. 181 (2020) http://dx.doi.org/10.1016/j.scriptamat.2020.02.017.

[29] W. Hu, X. Niu, L. Li, S. Yun, Z. Yu, Q. Pei, Intrinsically stretchable transparent electrodes based on silver-nanowire–crosslinked-polyacrylate composites, Nanotechnology 23 (34) (2012) http://dx.doi.org/10.1088/0957-4484/23/34/344002.

[30] F. Xu, Y. Zhu, Highly conductive and stretchable silver nanowire conductors, Adv. Mater. 24 (37) (2012) http://dx.doi.org/10.1002/adma.201201886.

[31] S. Aghazadehchors, V.H. Nguyen, D. Muñoz-Rojas, C. Jiménez, L. Rapenne, N.D. Nguyen, D. Bellet, Versatility of bilayer metal oxide coatings on silver nanowire networks for enhanced stability with minimal transparency loss, Nanoscale 11 (42) (2019) http://dx.doi.org/10.1039/c9nr05658k.

[32] N. Charvin, J. Resende, D.T. Papanastasiou, D. Muñoz-Rojas, C. Jiménez, A. Nourdine, D. Bellet, L. Flandin, Dynamic degradation of metallic nanowire networks under electrical stress: A comparison between experiments and simulations, Nanoscale Adv. 3 (3) (2021) http://dx.doi.org/10.1039/d0na00895h.

[33] J.-Y. Noh, S.-H. Ha, G.R. Jeon, J.-M. Kim, Geometrical and electrical modulation of cracked metal films based on metal nanowire/elastomer composites for high-performance wearable strain sensing, Compos. Sci. Technol. 230 (2022) http://dx.doi.org/10.1016/j.compscitech.2022.109738.

[34] C.W. Wang, L. Berhan, A.M. Sastry, Structure, mechanics and failure of stochastic fibrous networks: Part I - Microscale considerations, J. Eng. Mater. Technol. 122 (4) (2000) http://dx.doi.org/10.1115/1.1288769.

[35] C.W. Wang, A.M. Sastry, Structure, mechanics and failure of stochastic fibrous networks: Part II - Network simulations and application, J. Eng. Mater. Technol. 122 (4) (2000) http://dx.doi.org/10.1115/1.1288768.

[36] S. Kirkpatrick, Percolation and conduction, Rev. Modern Phys. 45 (4) (1973) http://dx.doi.org/10.1103/revmodphys.45.574.

[37] M. Žeželj, I. Stanković, From percolating to dense random stick networks: Conductivity model investigation, Phys. Rev. B 86 (13) (2012) http://dx.doi.org/10.1103/physrevb.86.134202.

[38] C. Gomes da Rocha, H.G. Manning, C. O'Callaghan, C. Ritter, A.T. Bellew, J.J. Boland, M.S. Ferreira, Ultimate conductivity performance in metallic nanowire networks, Nanoscale 7 (30) (2015) http://dx.doi.org/10.1039/c5nr03905c.

[39] C. Forró, L. Demkó, S. Weydert, J. Vörös, K. Tybrandt, Predictive model for the electrical transport within nanowire networks, ACS Nano 12 (11) (2018) http://dx.doi.org/10.1021/acsnano.8b05406.

[40] A. Behnam, V.K. Sangwan, X. Zhong, F. Lian, D. Estrada, D. Jariwala, A.J. Hoag, L.J. Lauhon, T.J. Marks, M.C. Hersam, E. Pop, High-field transport and thermal reliability of sorted carbon nanotube network devices, ACS Nano 7 (1) (2012) http://dx.doi.org/10.1021/nn304570u.

[41] T. Kim, A. Canlier, G.H. Kim, J. Choi, M. Park, S.M. Han, Electrostatic spray deposition of highly transparent silver nanowire electrode on flexible substrate, ACS Appl. Mater. Interfaces 5 (3) (2013) http://dx.doi.org/10.1021/am3023543.

[42] D. Kim, J. Nam, Electrical conductivity analysis for networks of conducting rods using a block matrix approach: A case study under junction resistance dominant assumption, J. Phys. Chem. C 124 (1) (2019) http://dx.doi.org/10.1021/acs.jpcc.9b07163.

[43] E.K. McCarthy, A.T. Bellew, J.E. Sader, J.J. Boland, Poisson's ratio of individual metal nanowires, Nat. Commun. 5 (1) (2014) http://dx.doi.org/10.1038/ncomms5336.

[44] Y. Sun, B. Mayers, T. Herricks, Y. Xia, Polyol synthesis of uniform silver nanowires: A plausible growth mechanism and the supporting evidence, Nano Lett. 3 (7) (2003) http://dx.doi.org/10.1021/nl034312m.

[45] T.-H. Chang, G. Cheng, C. Li, Y. Zhu, On the size-dependent elasticity of penta-twinned silver nanowires, Extreme Mech. Lett. 8 (2016) http://dx.doi.org/10.1016/j.eml.2016.03.007.

[46] G.Y. Jing, H.L. Duan, X.M. Sun, Z.S. Zhang, J. Xu, Y.D. Li, J.X. Wang, D.P. Yu, Surface effects on elastic properties of silver nanowires: Contact atomic-force microscopy, Phys. Rev. B 73 (23) (2006) http://dx.doi.org/10.1103/physrevb.73.235409.

[47] ACS Material, last accessed August 2023. https://www.acsmaterial.com.

[48] Novarials, last accessed August 2023. https://www.novarials-store.com.

[49] Sigma-Aldrich (Merck), last accessed August 2023. https://www.sigmaaldrich.com/US/en.

[50] J.R. Greer, J.T.D. Hosson, Plasticity in small-sized metallic systems: Intrinsic versus extrinsic size effect, Prog. Mater. Sci. 56 (6) (2011) http://dx.doi.org/10.1016/j.pmatsci.2011.01.005.

[51] C.R. Weinberger, W. Cai, Plasticity of metal nanowires, J. Mater. Chem. 22 (8) (2012) http://dx.doi.org/10.1039/c2jm13682a.

[52] F. Niekiel, E. Spiecker, E. Bitzek, Influence of anisotropic elasticity on the mechanical properties of fivefold twinned nanowires, J. Mech. Phys. Solids 84 (2015) http://dx.doi.org/10.1016/j.jmps.2015.08.004.

[53] D. Kim, J. Choi, J. Nam, Image analysis for measuring rod network properties, Meas. Sci. Technol. 26 (12) (2015) http://dx.doi.org/10.1088/0957-0233/26/12/125601.

[54] Y.Y. Tarasevich, I.V. Vodolazskaya, A.V. Eserkepov, V.A. Goltseva, P.G. Selin, N.I. Lebovka, Simulation of the electrical conductivity of two-dimensional films with aligned rod-like conductive fillers: Effect of the filler length dispersity, J. Appl. Phys. 124 (14) (2018) http://dx.doi.org/10.1063/1.5051090.

[55] X.-F. Wu, Y.A. Dzenis, Elasticity of planar fiber networks, J. Appl. Phys. 98 (9) (2005) http://dx.doi.org/10.1063/1.2123369.

[56] R. Cook, D. Malkus, M. Plesha, R. Witt, Concepts and Applications of Finite Element Analysis, fourth ed., John Wiley and Sons, 2002.

[57] J. Li, S.-L. Zhang, Finite-size scaling in stick percolation, Phys. Rev. E 80 (4) (2009) http://dx.doi.org/10.1103/physreve.80.040104.

[58] A. Leach, M. McDowell, K. Gall, Deformation of top-down and bottom-up silver nanowires, Adv. Funct. Mater. 17 (1) (2007) http://dx.doi.org/10.1002/adfm.200600735.

[59] Y. Gao, Y. Fu, W. Sun, Y. Sun, H. Wang, F. Wang, J. Zhao, Investigation on the mechanical behavior of fivefold twinned silver nanowires, Comput. Mater. Sci. 55 (2012) http://dx.doi.org/10.1016/j.commatsci.2011.11.005.

[60] M. Goudarzi, A. Simone, Discrete inclusion models for reinforced composites: Comparative performance analysis and modeling challenges, Comput. Methods Appl. Mech. Engrg. 355 (2019) http://dx.doi.org/10.1016/j.cma.2019.06.026.

[61] M. Goudarzi, D. Grazioli, A. Simone, An efficient computational approach for three-dimensional modeling and simulation of fibrous battery electrodes, Internat. J. Numer. Methods Engrg. 123 (7) (2022) http://dx.doi.org/10.1002/nme.6881.